Asymmetry and global instability of real minivan wakes

G. Bonnavion[a,*], O. Cadot[b], V. Herbert[c], S. Parpais[d], R. Vigneron[e], J. Délery[e]

[a] *IMSIA, ENSTA-ParisTech, UMR 9219 CNRS, 828 Boulevard des Maréchaux, 91762 Palaiseau Cedex, France*
[b] *University of Liverpool, School of Engineering, Liverpool L69 BX7, United Kingdom*
[c] *Groupe PSA, Route de Gisy, 78140 Vélizy-Villacoublay, France*
[d] *Renault, 1 avenue du Golf, 78280 Guyancourt, France*
[e] *GIE-S2A, 2 Avenue Volta, 78180 Montigny-le-Bretonneux, France*

Abstract

Three real minivan cars are investigated through base pressure distribution, force balance measurements and velocity measurements. Discontinuous transitions of permanent wake reversal and bistable dynamics are observed varying ground clearance, pitch and yaw, with open and closed air-intake. These transitions prove that the cars are subjected to the same global z-instability as the square-back Ahmed body (M. Grandemange, M. Gohlke and O. Cadot, Physics of Fluids, **25**, 2013). The contribution of the global instability to the aerodynamic force coefficient is estimated....????. Eventually, a demonstrative experiment of a real minivan drag reduction is shown to be improved by a factor 2 with a direct passive control of the z-instability.

Keywords: turbulent flow, bluff body, cars aerodynamics, wake multistability, bistability, static asymmetric modes

1. Introduction

From the aerodynamics point of view minivan cars are bluff bodies with vertical blunt rear geometry responsible for a massive flow separation featuring a turbulent recirculation and an unsteady wake. For a better understanding of the flow physics aiming at improving their aerodynamic performances, simplified models such as the Ahmed squareback body [1] have been extensively studied over the last decades. The seeding work of [2, 3] showed the presence of static asymmetric states of the wake that permanently break the reflectional symmetry of the body. These states have been firmly confirmed since by numerous research teams working on squareback academic bodies both experimentally [4, 5, 6, 7, 8, 9, 10] and numerically [11, 12, 13]. These asymmetric wake states are reminiscent of a global steady instability that appears for a critical Reynolds number through a pitchfork bifurcation in the laminar regime [2, 13]. At the critical

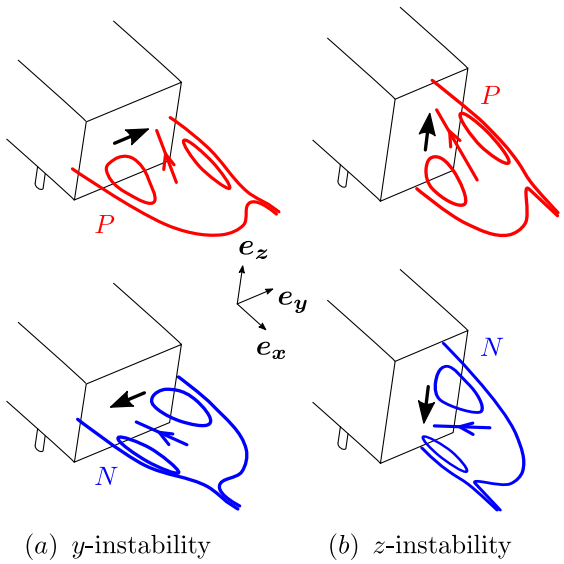

Figure 1: Sketches of the recirculating bubbles for the y-instability (a) and z-instability (b) interpreted from the mean wake measurements of [14]. Thick arrows display the corresponding base pressure gradients defining the state P (positive) or N (negative) depending on its sign.

*Corresponding author
Email address:
guillaume.bonnavion@ensta-paristech.fr (G. Bonnavion)

Reynolds number (few hundreds), the basic flow that respects all the symmetries becomes unstable (i.e. not observable), and the two asymmetric states become steadily stable, these P and N states are illustrated in figure $1(a)$. Depending on the initial flow condition and the residual imperfections, only one state is selected in the laminar regime. As the Reynolds number is increased and the flow becomes turbulent, the reflectional symmetry is statistically restored through bistable long-time dynamics [3, 4] consisting in random switching between state P and state N. These states have been observed for the Ahmed body at the industrial flow scale with rotating wheels and road effet [15]. As reported in [14, 16], there is a critical ground clearance c_c below which the wake is symmetric and the asymmetric states suppressed. This ground clearance is approximately $c_c \approx 0.1W$ at the Reynolds number $\mathrm{Re}_W = 4.5 \times 10^4$ based on the body width W [14]. For increasing Reynolds numbers, the critical ground clearance decreases continuously as $\mathrm{Re}_W^{-1/6}$ [16]. Hence, sufficient flow at the bottom edge of the base is actually necessary for the global wake instability. Similar conclusion was reported by [17] changing the under-body porosity keeping a constant ground clearance. For minivan cars, the ground clearance is always high enough to not have to consider any stabilization effects due to any under-body flow rate deficit.

Later, [14] showed the importance of the rectangular base aspect ratio that can trigger either left/right asymmetric states when the base is wider than it is tall or top/bottom asymmetric states when the base is taller than it is wide. They are respectively called y- and z-instabilities, where y and z refer to the wake asymmetry directions as depicted in figure 1. Although the y-instability corresponds to a pure reflectionnal symmetry-breaking, the z-instability does not, because of the ground and the body supports [14]. The consequence is that z-instability in the turbulent regime has no reason to lead to bistable dynamics, since there is no symmetry to restore as for the y-instability. Hence it is not an easy task to diagnose a z-instability, since in the absence of a bistable dynamics, the permaanent vertical wake assymmetry can be legitimately ascribed to the car top/bottom asymmetry and ground proximity. Apart from the study of [14], there are only few studies [18, 19] of the z-instability.

Beside, the only case of bistable dynamics of a real minivan car reported in the literature with a Renault Kangoo [20] showed huge fluctuations of lift between two most probable values for the car in yaw at 4°. This case was deeply characterize in [21] who also mentioned the importance of the flow through the air-intake. They interpreted these bistable dynamics by the global z-instability as in [14] although the base aspect ratio would indicate a y-instabillity rather than a z-instabillity in the framework of Ahmed bodies of [14]. However, real minivans are much more complex geometries than Ahmed bodies and the role of thick wheels [22] and asymmetrical car shape are other parameters that influence the global instability type.

A clear diagnose of z-instability was recently presented in [19] for a flat backed Ahmed body. In the presence of the instability, the vertical component of the base pressure gradient (and lift) undergoes discontinuous transitions when pitch, yaw and ground clearance are varied. At each transition, the dynamics is bistable due to a symmetry compensation effect in the z-direction, basically related to a intensity modification of the under-body flow. In yaw, this change is produced by the wake of the front leeward wheel. In addition, the authors propose a relationship between the cross flow coefficients and the base pressure gradient components with an explicit contribution of the global instability strength.

The aim of this paper is to make use of the same strategy of [19] to prove that the wakes of the four real cars at full flow scale; the Peugeot 5008, the Peugeot Partner, the Citroën Berlingo and the Renault Kangoo are permanently subjected to a z-instability. To illustrate the impact of the global instability on the aerodynamics performance, a passive control of the instability is achieved for an improved drag reduction of the Peugeot Partner.

The paper is organized as follows. The experimental setup is described in § 2. Results in § 3 are split into four parts, § 3.1 presents the baselines characteristics, § 3.2 investigates the wake response to variations of ground clearance, pitch and yaw angles, § 3.3 assesses the global instability contribution to the aerodynamics force and § 3.4 evidences a beneficial impact of controlling the instability. Finally, a concluding discussion § 4 ends the paper.

2. Experiments

2.1. Wind tunnel and minivan models

The experiments are conducted in the full-scale wind tunnel of the GIE-S2A (*Souffleries Aroacoustiques Automobiles*, Montigny-le-Bretonneux, France) dedicated to ground vehicles' aerodynamics. A full description of the facility can be found in [23]. Among the main characteristics, the test section is a 3/4-open jet. A rolling belt moving at the air-speed between the wheels mimics the road and four wheel-spinners simulate realistic driving conditions. The boundary layer is controlled by suction upstream of the vehicle.

Three blunt based vehicles are considered in this study: a Peugeot 5008 (figure 2*a*), a Peugeot Partner (figure 2*b*) and a Citroën Berlingo (figure 2*c*). The characteristic dimensions of the vehicles can be found in table 1 in which the Renault Kangoo studied in [20, 21] is also mentioned.

The ground proximity is adjusted owing four vertical pneumatic masts fixed to the car under-body near each wheels and to the force balance. The car can be independently pushed-up or pull-down near each axle. The minimum and maximum heights are limited by the springs of the car suspension system. The ground proximity is measured by the distances λ_f between the ground and the top of the wheel-arch for the front axle and λ_r for the rear axle as indicated in figure 2(d). A pitch angle α can be computed from these two heights and the wheel-base Λ such that:

$$\tan\alpha = \frac{\lambda_f - \lambda_r}{\Lambda}. \tag{1}$$

Positive pitch angles correspond to car nose-up and negative to car nose-down. A large turntable supports the force balance, the moving belt and the car to adjust the yaw angle.

The base height H and the free-stream velocity U_∞ are chosen as the characteristic dimensions of the problem and any quantities with superscript * are non-dimensionalized using H and U_∞ (for instance the non dimensional time is $t^* = tU_\infty/H$). The Reynolds number is thus defined as $\mathrm{Re} = \frac{U_\infty H}{\nu}$, ν being the kinematic viscosity of air. Two different free-stream velocities are used for the tests: $U_\infty = 38.9 \pm 0.1$ m.s^{-1} for the Peugeot 5008 and Partner and $U_\infty = 33.3 \pm 0.1$ m.s^{-1} for the Citroën Berlingo. The temperature is regulated at 20°C. In these regimes, the flow non-uniformity of the facility lies below 0.4%.

The vehicles are either tested in real driving conditions with the front air-intake dedicated to the engine and breaks cooling system open, or obstructed to avoid air through the body as for academic Ahmed bodies [1].

2.2. Measurements of wall pressure, aerodynamic force and velocity fields

The vehicle's base pressure distribution is estimated owing to N pressure taps distributed over the car's base (Peugeot 5008, $N = 30$; Peugeot Partner, $N = 30$; Citroën Berlingo, $N = 24$) and connected to a Scanivalve ZOC22b pressure scanner operated with a GLE/SmartZOC100 electronics at a sampling frequency of 200 Hz. The actual cut-off frequency of the pressure measurement due to the vinyl tubing length connecting the pressure tap to the scanner is approximately 20 Hz. Nonetheless, it is sufficient to capture the long-time dynamics of the wake that occur at lower frequencies than few Hertz [20, 21]. The location of the base pressure taps can be found for each of the vehicles in figure 2($a-c$). The scanner actually gives the differential pressure $p - p_\infty$, where the static pressure p_∞ is obtained from the upstream section of the facility. This differential pressure is expressed as the pressure coefficient :

$$c_p = \frac{p - p_\infty}{\frac{1}{2}\,\rho\,U_\infty^2}, \tag{2}$$

where ρ is the air density.

A base pressure gradient $\mathbf{g}^*$ is computed using the taps indicated as A, B, C and D in figure 2($a-c$). The procedure is the same for all vehicles. The two Cartesian components are computed as:

$$g_y^* = \frac{1}{2} \times \left[\frac{c_p(y_A^*, z_A^*) - c_p(y_B^*, z_B^*)}{y_A^* - y_B^*} + \frac{c_p(y_C^*, z_C^*) - c_p(y_D^*, z_D^*)}{y_C^* - y_D^*} \right] \tag{3}$$

and:

$$g_z^* = \frac{1}{2} \times \left[\frac{c_p(y_A^*, z_A^*) - c_p(y_C^*, z_C^*)}{y_A^* - y_C^*} + \frac{c_p(y_B^*, z_B^*) - c_p(y_D^*, z_D^*)}{y_B^* - y_D^*} \right] \tag{4}$$

We use both the Cartesian and polar form of $\mathbf{g}^*$ respectively denoted (g_y^*, g_z^*), referred to as horizontal and vertical gradient components, and (g_r^*, φ), referred to as strength and orientation.

Table 1: Dimensions of the vehicles and Reynolds numbers. The superscript * indicates lengths expressed in unit of H. The given values for the front and rear wheel-arch heights are defining the baselines. The Renault Kangoo is reported from [20, 21].

Dimension	5008	Kangoo [20, 21]	Partner	Berlingo
Base height H:	1.320 m	1.480 m	1.480 m	1.480 m
Base aspect ratio W^*:	1.212	1.115	1.121	1.121
Wheelbase Λ^*:	2.114	1.822	1.843	1.843
Front wheel-arch height λ_f^*:	0.519	0.488	0.480	0.480
Rear wheel-arch height λ_r^*:	0.539	0.488	0.480	0.480
Natural pitch angle α:	$-0.55°$	$0°$	$0°$	$0°$
Frontal surface S^*:	1.578	1.297	1.297	1.297
Vehicle's length L^*:	3.431	2.893	2.959	2.959
$\mathrm{Re} = \frac{U_\infty H}{\nu}$:	5.13×10^6	4.93×10^6	5.76×10^6	5.13×10^6

Force measurements are recorded at the sampling frequency of 10 Hz with a six-components force balance provided by Schencker GmbH and located below the wind tunnel floor. The unsteady forces f_x, f_y and f_z, corresponding respectively to drag, side force and lift are made non-dimensional into the coefficients :

$$c_i = \frac{f_i}{\frac{1}{2}\ \rho\ S\ U_\infty^2}, \tag{5}$$

with S being the vehicle's projected frontal area.

Pressure distribution $c_p(y, z, t)$ and force coefficients $c_i(t)$ are simultaneously recorded during $2-4$ minutes. Recorded signals are afterwards low pass filtered using a sliding window of 0.5 s corresponding to a much lower cut-off frequency than that of both measurements in order to obtain identical frequency resolution for pressure and force time series. Before each set of experiments, a no-wind acquisition is performed whose averaged value is subtracted to the actual measurements to correct any offset.

Measurements in the wake use three 18 holes spherical probes mounted on a three-axis traversing system [23]. The probes are "omniprobe" models from Aeroprobe Corporation having diameters of 9.53 mm. The measurement is performed continuously at an acquisition rate of 2.5 Hz while the traversing system is moving at a constant speed of 75 mm.s^{-1}. Hence, one measurement point is obtained each 30 mm that sets the spatial resolution. It gives the mean velocities U_x, U_y and U_z and its gradients after processing as well as the static pressure. The precision of the velocity is given by the manufacturer to be less than 1% of the measured velocity modulus, and the angular precision to be less than $0.4°$. The automatic displacement allows to get these data in planes iso-x, iso-y or iso-z. In the present experiments, the mean wake is investigated in a vertical plane $y^* = 0$ and displayed as the modulus of the velocity component in that plane, $U_{xz}^* = \sqrt{U_x^{*2} + U_z^{*2}}$ superimposed to the streamlines computed from (U_x^*, U_z^*).

In the following, for any time dependant variable x, capital letter X refers to as time averaged value and $X' = \sqrt{(x - X)^2}$ to the mean fluctuations (standard deviation). We recall that superscript * denotes a quantity made non dimensional using H and U_∞.

3. Results

The results section is organized as follows. We first characterize the baselines flow in § 3.1 for both air intake systems either open or closed. Wake reversals and bistable dynamics are evidenced varying ground clearance in § 3.2.1, pitch angle in § 3.2.2 and yaw angle in § 3.2.3. The strength of the global instability contributing the force coefficient is then investigated in § 3.3 and eventually some demonstrative passive manipulations of the instability is investigated to prove its significant aerodynamic impact in § 3.4.

3.1. Baselines for open and closed air intake

The baseline is defined for the vehicles having their natural wheel-arch heights and pitch angle as given in table 1 and aligned with the incoming flow ($\beta = 0°$). We consider two baseline cases. The first one corresponds to the air-intake system that is not modified so that air can flow through as required by engine cooling. The corresponding main

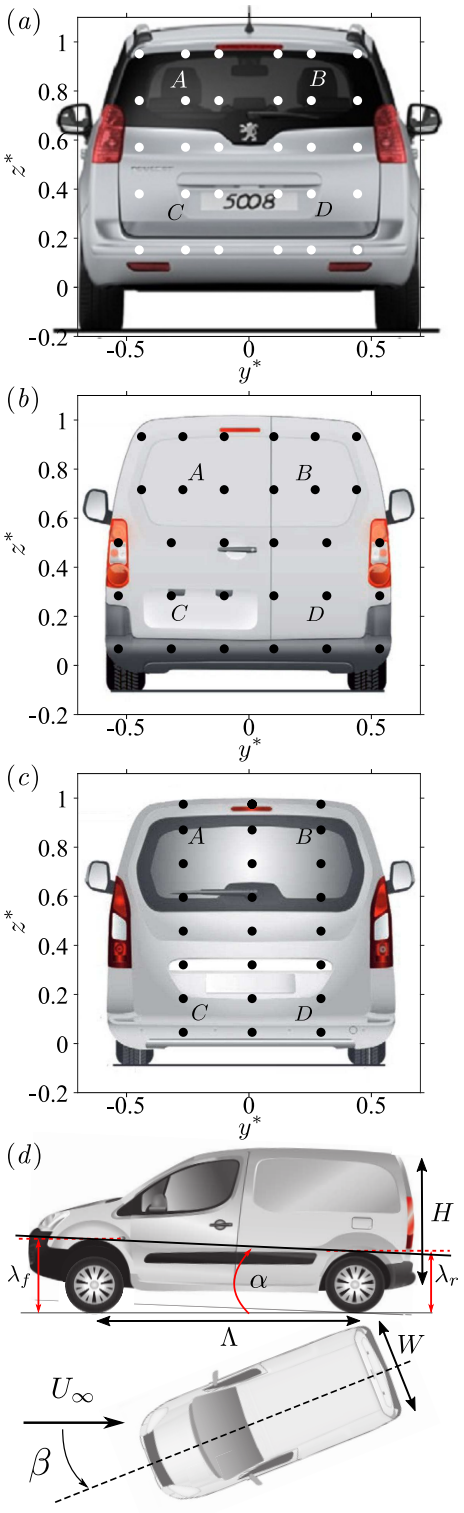

Figure 2: Vehicles with pressure tap locations and geometrical alignments. (a) Peugeot 5008, (b) Peugeot Partner and (c) Citroën Berlingo. (d) Definition of the distances λ_f, λ_r, pitch angle α (not to scale) and yaw angle β. Lengths are expressed in the non dimensional unit $y^* = y/H$, $z^* = z/H$.

Table 2: Aerodynamics mean coefficients for baseline configurations of the four vehicles with open air-intake.

Vehicle	C_b	C_x	C_y	C_z	State
5008	0.128	0.278	0.003	0.010	P
Kangoo	0.125	0.347	0.004	0.012	P
Partner	0.182	0.339	0.003	0.017	P
Berlingo	0.183	0.336	0.001	0.017	P

Table 3: Aerodynamics mean coefficients for baseline configurations of the four vehicles with closed air-intake.

Vehicle	C_b	C_x	C_y	C_z	State
5008	0.128	0.258	...	0.015	P
Kangoo	0.156	0.334	...	0.029	N
Partner	0.173	0.318	...	0.002	P
Berlingo	0.172	0.312	...	0.014	P

aerodynamic force coefficient displayed in table 2 shows that all cars with open air intake develop a positive lift coefficient C_z with a negligible side force C_y, never strictly null as a direct consequence of residual asymmetries of the underbodies, engine compartment...

For the second case, the front air intake grid at the fore-body is sealed with wide adhesive tape (see illustration in [21]) obliging the flow to go around the body as for academic Ahmed bodies. The closure effect can be seen comparing the aerodynamic force coefficient in table 2 to those obtained in table 3. The closure produces a substantial drag reduction from 7.2% for the 5008, 7.1% for the Berlingo, 6.2% for the Partner to only 3.7% for the Kangoo. This changes are considerable at a vehicle's scale in view of fuel-efficiency and carbon emissions reduction. The drag reduction is not correlated to the base suction which indicates that the wake is not involved. The drag reduction must be explained by the large head loss as the air flows through the engine compartment.

The air intake closure has only little effects on the base pressure distribution of the 5008, the Berlingo and the Partner as shown in figures $3(a, b, c)$ respectively. They all show an almost vertical and positive base pressure gradient with small fluctuations in orientation and modulus. They are well defined states with turbulent fluctuations, but with no bi-stable dynamics. We will then qualify the cor-

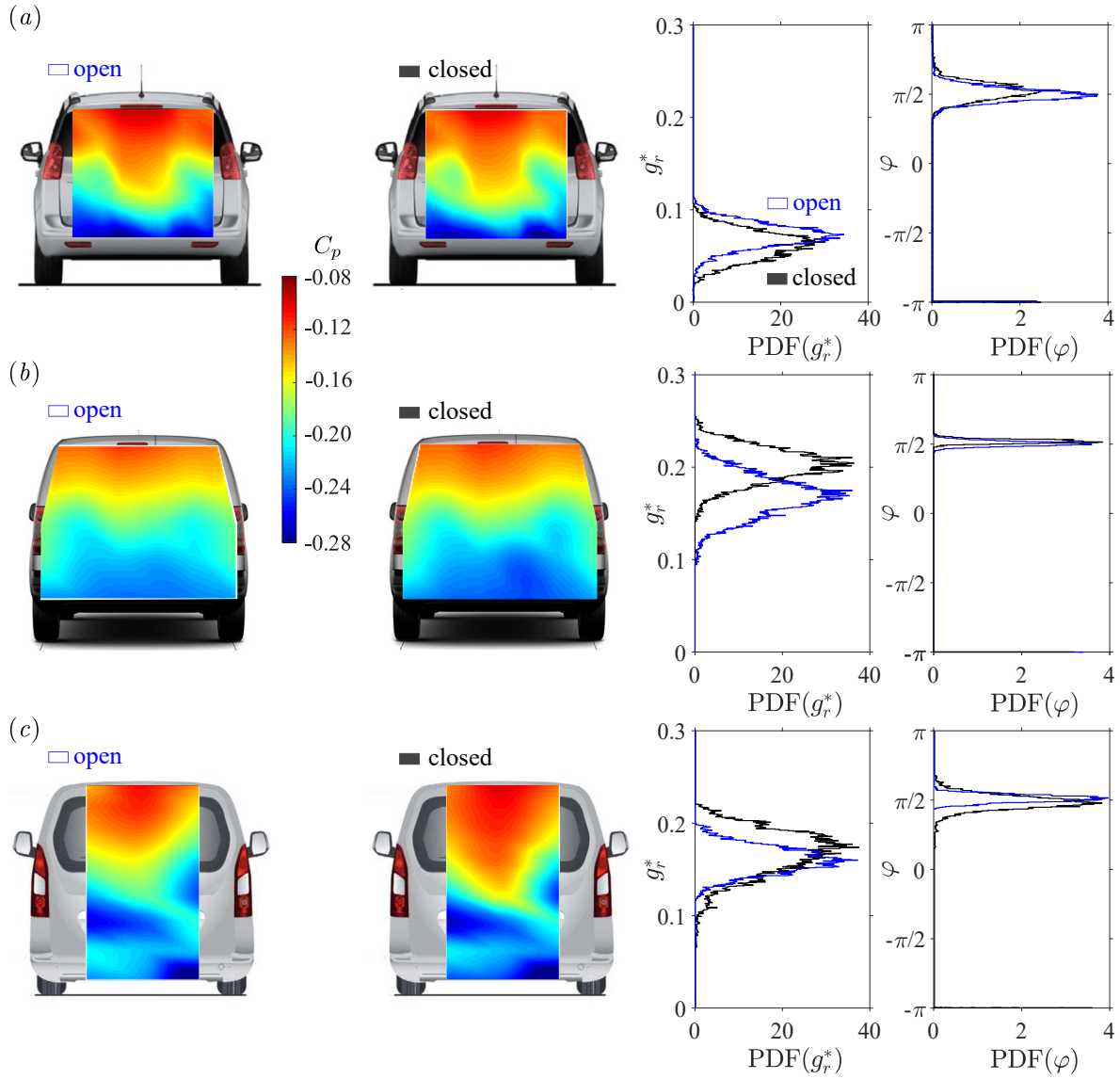

Figure 3: Baselines properties for (a) Peugeot 5008, (b) Peugeot Partner and (c) Citron Berlingo. Mean base pressure distributions $C_p(y^*, z^*)$ with front air-intake open (left column) and closed (right column). Corresponding base pressure gradient statistics displayed as modulus (left column) and phase orientation (right column) for front air-intake open (blue line) and closed (black line).

responding flows at the base as P states in tables 2 and 3. On the contrary to these cars, the air-intake closure of the Kangoo was observed to produce a permanent wake reversal in [21] from state P to a state N with negative vertical base pressure gradient. This global change of the wake is accompanied by the large increase of lift and base suction in table 3. The wake reversal is also at the origin of the small drag reduction of 3.7% obtained with the Kangoo compared to the $6\% - 7\%$ of the other cars.

In the following, we aim at revealing hypothetical discontinuous transitions towards a reversed wake state by changing the ground clearance, the pitch and the yaw angles.

3.2. Wake reversals and bistable dynamics

This section presents base pressure gradient responses to variations of the pitch α and the yaw angle β. The responses are assessed as in [19] through the statistics of the base pressure gradient consider-

ing each component of coordinate systems $(g_y^*,\ g_z^*)$ by representing its probability density function f normalized by its most probable value. The resulting plots are two two-dimensional sensitivity maps for each of the two geometrical configurations varying the parameter $q = \alpha$ or β: $f(q, g_y^*)$, $f(q, g_z^*)$. The mean velocity fields of the wake are investigated for chosen specific configurations identified in the sensitivity maps.

3.2.1. Ground clearance variations

The ground clearance experiment is conducted with the Peugeot 5008 only. Since the Ahmed body that is subjected to the z-instability [14, 19] switches from a P state to a N state when the ground clearance is increased, we simply apply the largest ground clearance accessible to the 5008. The car is then lifted up by 81 mm on each axle. The base pressure distribution $C_p(y^*, z^*)$ shown in figure $4(a)$ and the base gradient statistics in figures $4(b)$ actually indicates a negative vertical pressure gradient for this highest ground clearance. Unlike for the experiments with the simplified geometry reported in [14, 19], the modulus of the gradient g_r^* is affected by the wake orientation and reduced by almost a factor of two in state N compared to the state P. A smaller modulus of similar magnitude for the state N was also reported for the Kangoo by [21].

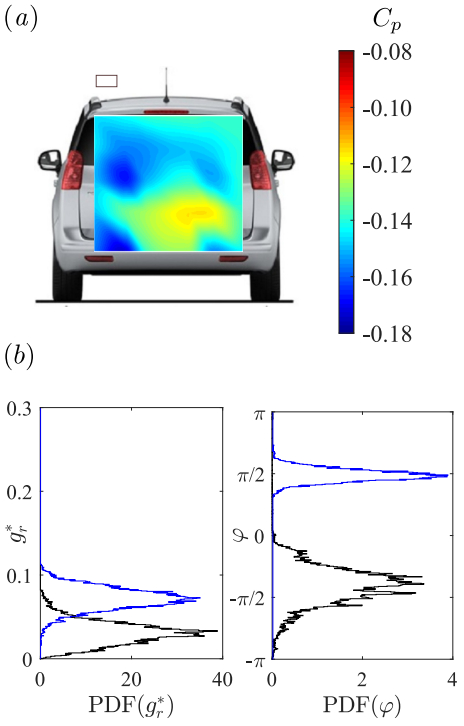

Figure 4: Peugeot 5008 at $\lambda_f^* = 0.580$, $\lambda_r^* = 0.600$. Mean base pressure distribution $C_p(y^*, z^*)$ (a). Statistics (b) of the modulus g_r^* and the phase φ of the base pressure gradient. The blue curves in (b) are the corresponding baseline with open air-intake.

No sensitivity experiments to the ground clearance have been undertaken to investigate the discrete or continuous nature of the transition between the two states. These have been realized in the following changing pitch and yaw.

3.2.2. Pitch variations

Pitch angle sensitivity experiments are conducted with the Peugeot 5008 with open air-intake and Berlingo with closed air-intake. An explored range of $\alpha \in [-0.55°, 1.45°]$ is obtained for the 5008 by changing the rear axle clearance only from the baseline. For the berlingo, the front wheel-arch is placed at $\lambda_f^* = 0.534$ and the rear axle clearance is modified to explore the range $\alpha \in [1.9°, 2.3°]$. The resulting sensitivity maps of the 5008 are given in figure 5, and these of the berlingo in figure 6. These figures display branches that locate the most probable value of the variable. For both cars, the horizontal component g_y^* in figure $5(a)$ and figure $6(a)$ fluctuates around zero as expected by the reflectional symmetry of the turbulent wake. An unexpected behaviour is observed on the vertical component of the gradient g_z^* in figure $5(b)$ and in figure $6(b)$. The branch observed for low pitches at about $g_z^* \simeq 0.1$ switches as a clear discontinuous transition to a lower branch at about $g_z^* \simeq -0.05$. It is remarkable that the value of each branch keeps an almost constant value independently to the pitch angle variation. These two values define uniquely two states of the wake, the upper branch being the P state and the lower the N state. It is in agreement with the Ahmed body subjected to the z-instability [19] that switches discontinuously from the P state to a N state by increasing positively the pitch angle. Although not reported in this paper, decreasing the pitch from the baseline for the 5008 and Berlingo lead to identical wake state as the baseline.

The mean base pressure distribution $C_p(y^*, z^*)$ of the Peugeot 5008 at the pitch $\alpha = 1.45°$ is shown in figure $7(a)$. It is very similar to the distribution observed with large ground clearance in figure $4(a)$ since they are both N states. The associated mean wake velocity field is shown in figure $7(b)$ and compared to the baseline at $\alpha = -0.55°$ in figure $7(c)$.

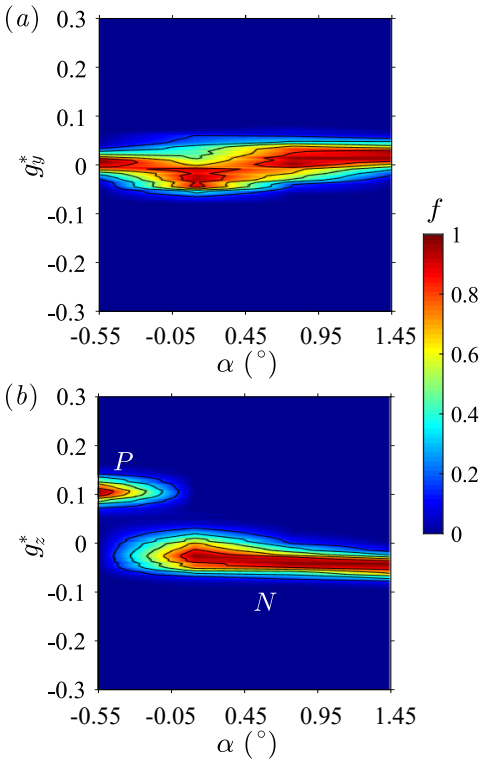

Figure 5: Base pressure gradient response to variations of the pitch angle α for the Peugeot 5008. Sensitivity maps (a) $f(\alpha, g_y^*)$, (b) $f(\alpha, g_z^*)$.

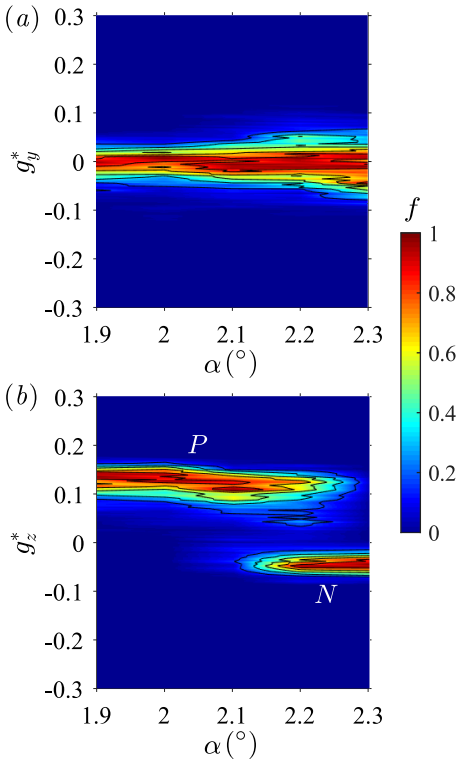

Figure 6: Base pressure gradient response to variations of the pitch angle α for the Berlingo with closed front air-intake. Sensitivity maps (a) $f(\alpha, g_y^*)$, (b) $f(\alpha, g_z^*)$.

With the negative pressure gradient in figure 7(b), the feedback flow in the recirculating bubble is orientated towards the bottom of the car, while it is orientated towards to top of the car for the positive gradient in figure 7(c). Identical observations are made for the Berlingo with closed air-intake in figure 8. The red vertical profile of the pressure coefficient in figure 8(a) indicates a negative vertical gradient for the pitch $\alpha = 2.3°$ while the blue profile shows a positive gradient for the pitch $\alpha = 1.9°$. The associated mean wake velocity field are respectively shown in 8(b) and 8(c). Again, the feedback flow orientation matches the sign of the vertical base pressure gradient indicating the wake reversal. Although the car configuration of the baseline with open air intake has a very different ground clearance, it is shown for comparison in 8(c). It presents the same orientation of the feedback flow as in 8(c) since both are P states, but more surprisingly, the bubble shape of the baseline appears as a mirror symmetry of that of the N state in 8(b).

The Partner displayed the same behaviour as the Berlingo in pitch with closed air intake. We also performed pitch experiment for both cars with open air-intake but never observed any wake reversals.

3.2.3. Yaw variations

A yaw angle sensitivity experiment is conducted for the Partner – with closed air-intake – starting from a bi-stable case obtained in pitching conditions with $\alpha = 2.1°, \beta = 0°$ similar to that observed with the Berlingo in figure 6(b) during the N and P branches switch around $\alpha = 2.2°$. The response of the base pressure gradient to the yaw variation is given in figure 9. Only positive values of the yaw angle β are considered in view of the quasi-symmetry of the problem.

The yaw breaks the reflectional symmetry and produces a significant variation of horizontal component of the pressure gradient g_y^* in figure 9(a). Nevertheless, the yaw is also able to trigger a discontinuous transition between two branches P and N on the vertical component in figure 9(b). However the most probable gradient of each branch is approximately larger by 30% the value of the 5008 in figure 5(b) or the Berlingo in figure 6(b). We have

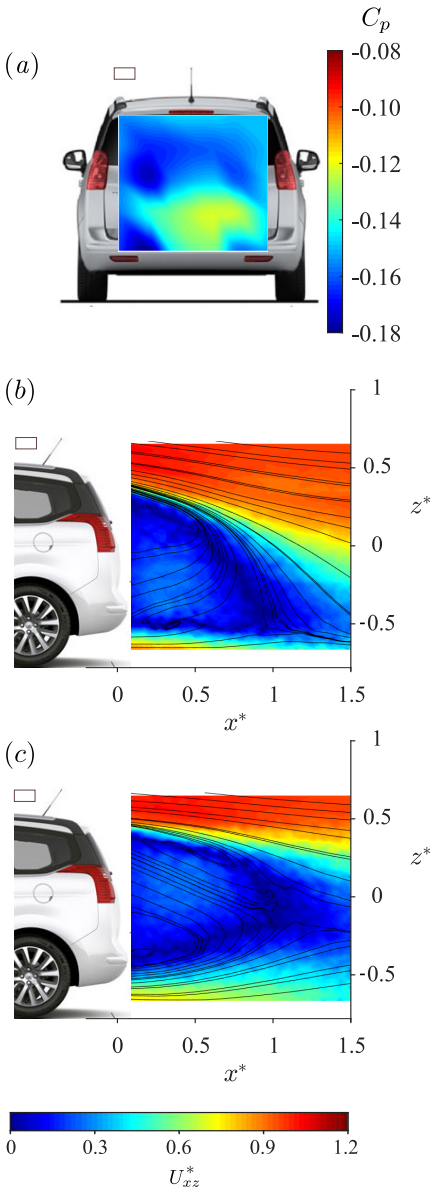

Figure 7: Wake reversals operated by the pitch for the Peugeot 5008. State N at $\alpha = 1.45°$: base pressure coefficient distribution (a), mean velocity field (b). State P at the baseline $\alpha = -0.55°$: mean velocity field (c).

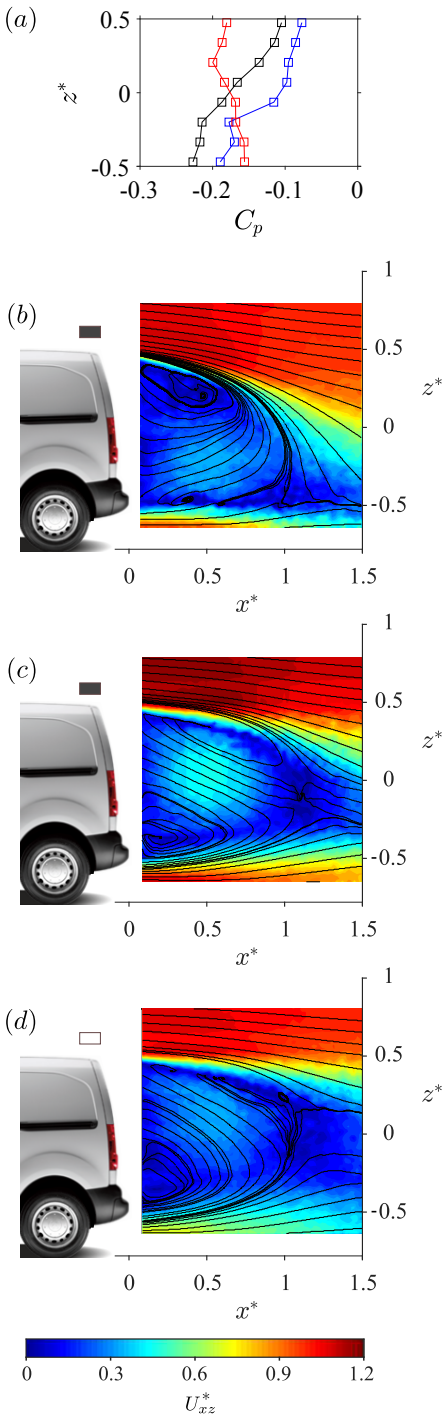

Figure 8: Wake reversals operated by the pitch for the Berlingo. State N with closed air-intake at $\alpha = 2.3°$: base pressure coefficient profile in red curve (a), mean velocity field (b). State P with closed air-intake at $\alpha = 1.9°$: base pressure coefficient profile in blue curve (a), mean velocity field (c). State P at the baseline with open air-intake ($\alpha = 0°$): base pressure coefficient profile in black curve (a), mean velocity field (d).

no clear explanation why the pressure gradients is so large for the Partner although the Berlingo and the Partner are not strictly identical (differences with the cargo door or the front design), and that the pressure sensors locations are different (figure 2c, d). We show the mean pressure distributions of the Partner for the yaw $\beta = -1°$ in figure 10. At this yaw, the exploration of the two states (as can be seen in figure 6b) create the

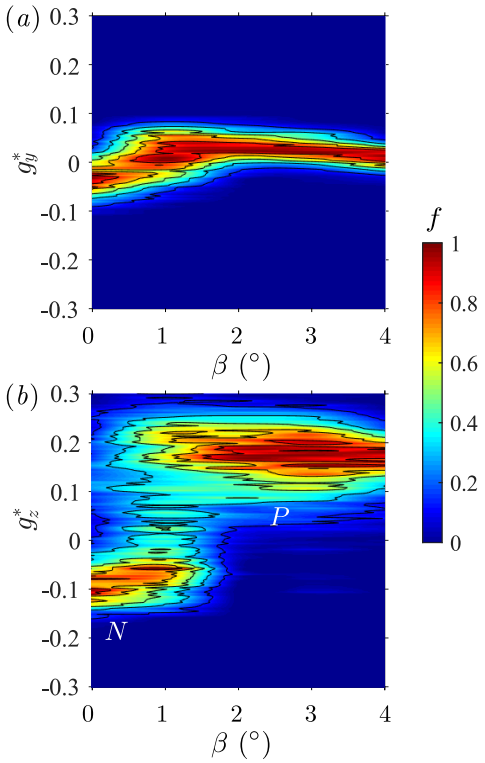

Figure 9: Base pressure gradient response to variations of the yaw angle β for the Partner with closed front air-intake. Sensitivity maps (*a*) $f(\beta, g_y^*)$, (*b*) $f(\beta, g_z^*)$.

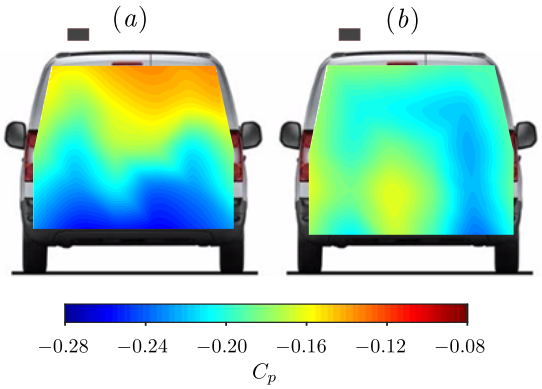

Figure 10: Conditionally averaged mean base pressure distributions $C_p(y^*, z^*)$ (see text) for states P (*a*) and N (*b*) of the Partner in yaw at $\beta = 1°$ and with closed front air-intake.

bi-stable dynamics. Simple conditional averaging based on the gradient sign gives the mean distribution associated with the P state in figure 10(*a*) and the N state in figure 10(*b*). We did not investigate velocity measurements for the yaw experiments.

3.3. Contribution of the global instability to the aerodynamics force

The relationship between the cross flow force and the base pressure gradient proposed in [19] for a flat blacked Ahmed body subjected to the z-instability will be tested on the data of the Berlingo in pitch (figure 6*b*) and the Partner in yaw (figure 9*b*). The relationships read for the side force and lift coefficients :

$$c_y(t^*) = C_y^B - \xi g_y^{*\prime}(t^*) \tag{6a}$$

$$c_z(t^*) = C_z^B - \xi g_z^*(t^*) \tag{6b}$$

The two quantities C_y^B and C_z^B are the time independent cross flow coefficients of the body without the z-instability. They are defining a basic flow assumed to be steady but depending on the pitch and yaw angles. These two force coefficients as well as the constant ξ are obtained by considering the temporal mean of (6):

$$C_y = C_y^B \tag{7a}$$

$$C_z = C_z^B - \xi G_z^* \tag{7b}$$

Hence, C_y^B is simply given by the mean side force coefficient of the vehicle as a result of the matching mechanism of the z-instability reported in [19]. The lift coefficient C_z^B of the basic flow and the constant ξ are obtained with a best fit involving the measurements of the mean lift C_z and mean vertical component of the base pressure gradient G_z^*. The mean force coefficients of the vehicles are shown as filled black circles for the Berlingo in pitch in figure 11(a, b) and the Partner in yaw in figure 12(a, b). The location of the most probables c_z, denoted by the thick black lines in figures 11(b) and 12(b), are extracted for clarity from the sensitivity maps $f(\alpha, c_z)$ of the Berlingo and $f(\beta, c_z)$ of the Partner. It clearly identifies the two branches P and N. In figures 11(b), C_z^B is assumed to be affine with α and the best fit gives:

$$C_z^B = 0.052\alpha - 0.036. \tag{8}$$

with $\xi = 1/5.3$. In figures 12(b), C_z^B is assumed to be quadratic with β (to respect the symmetry $\beta \to -\beta$) and the best fit gives:

$$C_z^B = 4 \times 10^{-4}\beta^2 + 0.078 \tag{9}$$

with $\xi = 1/6.5$. In both relations (8) and (9), angles are expressed in degrees. Using the results of the fits, the mean relationship (6b) is plotted as the

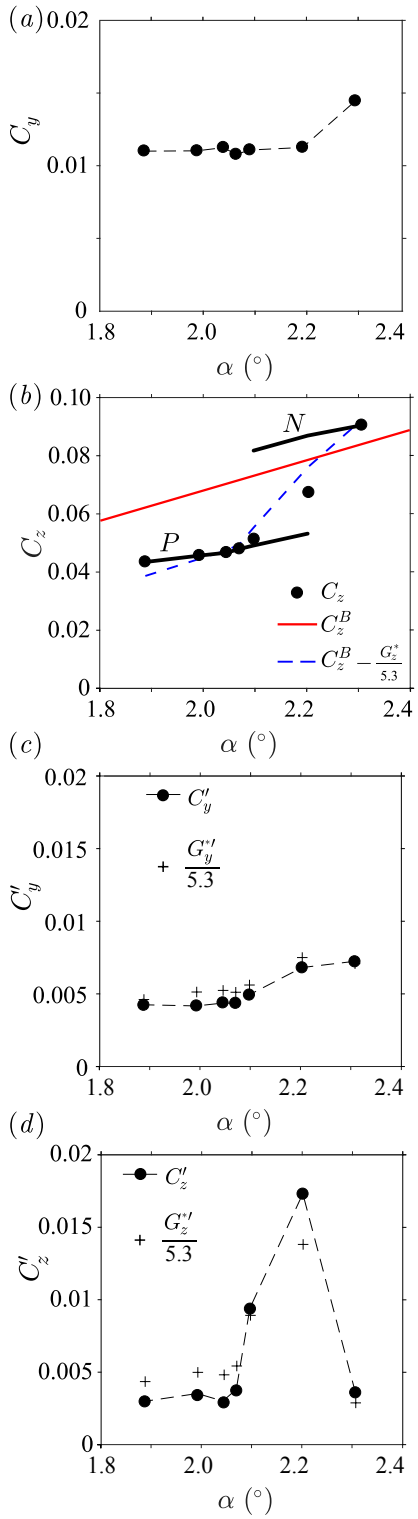

Figure 11: Pitch sensitivity analysis for the Berlingo: (a) mean side force coefficient, (b) mean (symbols) and most probable lift coefficients(thick black lines), *basic flow* lift coefficient C_z^B (red line) and mean lift computed from equation (6b) in blue dashed line. Mean fluctuation of (c) side force compared to horizontal pressure gradient, (d) lift compared to vertical base pressure gradient.

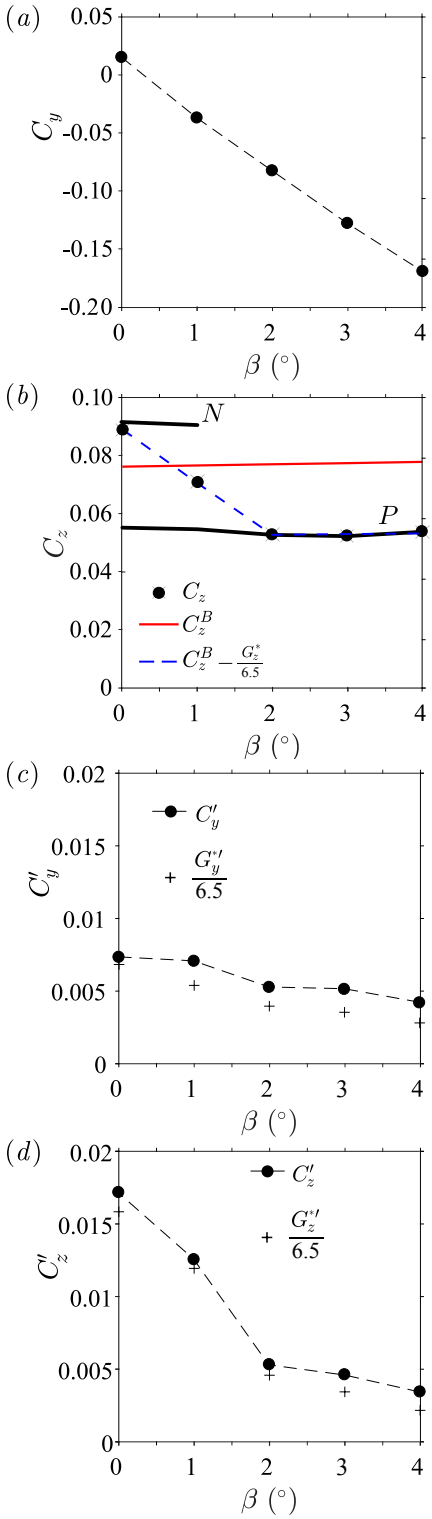

Figure 12: Yaw sensitivity analysis for the Partner: (a) mean side force coefficient, (b) mean (symbols) and most probable lift coefficients(thick black lines), *basic flow* lift coefficient C_z^B (red line) and mean lift computed from equation (6b) in blue dashed line. Mean fluctuation of (c) side force compared to horizontal pressure gradient, (d) lift compared to vertical base pressure gradient.

blue dashed lines in both figures 11(b) and 12(b), which satisfactorily matches the mean lift measurements. The mean fluctuation measurements C_y' and C_z' are also well recovered in figures 11(c,d) and 12(c,d) by the relation (6) yielding to :

$$C_y{}' = \xi G_y^{*\prime} \tag{10a}$$

$$C_z{}' = \xi G_z^{*\prime} \tag{10b}$$

Eventually, the time series of the measured instantaneous lift coefficient is compared to the model (6b) computed from the pressure gradient time-series using the basic flow coefficient and ξ found above. The comparison is shown in figure 13 during both bi-stable dynamics at $\alpha = 2.2°$ for the Berlingo and $\beta = 1°$ for the Partner. The relationship 6b deduced in [19] from the flat backed Ahmed bodies is indeed well checked for a complex real geometry at a real flow scale. We can conclude that the contribution of the instability to the lift force coefficient is similar for both cars; It is estimated from the difference between the basic flow coefficient and the branches of states P and N in both figures 11(b) and 12(b). It approximately corresponds to a strength of 0.012 for state N, and 0.024 for state P. It is a substantial contribution to the total aerodynamic force. They respectively represents about 3.5% and 7% of the drag or 70% and 140% of the lift of the baseline with open air-intake. Figure 14 shows the evolution of the mean drag coefficient during both pitch and yaw sensitivity experiments. [19] reported for the flat backed body that for both y- and z-instabilities the mean drag reaches a minimum at each transitions where the bi-stable dynamics occur, i.e. where the wake fluctuations are the largest. The explanation given in [5] being that switching events of the bistable dynamics have lower drag that the asymmetric states. This effect seems to be retrieve in figure 14 for real cars where local minima can be found around both transitions at 2.2° in pitch and 1° in yaw. Independently to this effect, conditional averaging operated on state P or N reveals different drags, with larger drag for state N than for state P. This difference was actually observable in the baselines of the Kangoo car whose drag is given in tables 2 and 3 for open and closed air-intake. While the other cars that remained in state P with closed air intake show almost no variation or small base suction reduction, the Kangoo base suction increases from $C_b = 0.125$ to $C_b = 0.156$ due to the switch from a P state to a N state. There could be a practical interest to

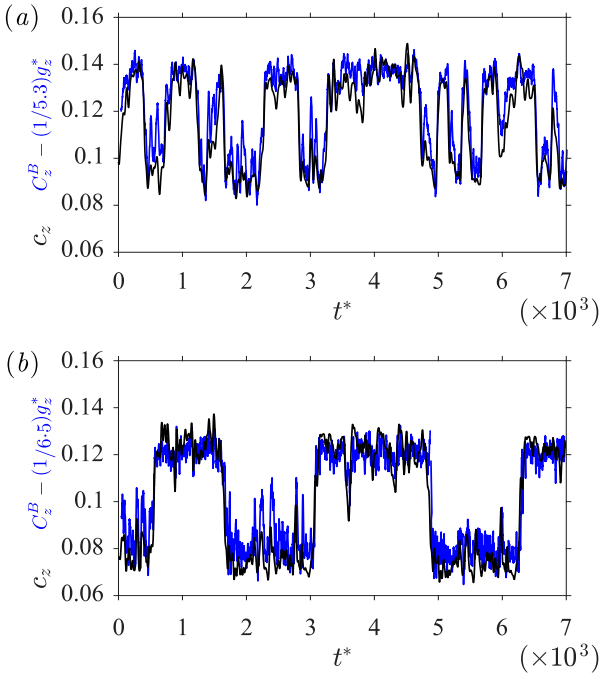

Figure 13: Time series of the lift coefficient $c_z(t^*)$ and reconstructed value from equation (6b) (see text) during bistable dynamics of the Berlingo in pitch at $\alpha = 2.2°$ (a) and the Partner in yaw at $\beta = 1°$ (b).

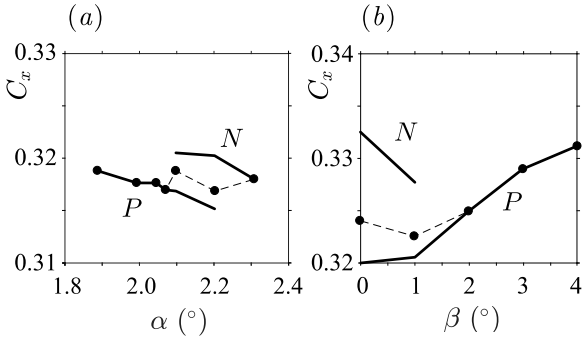

Figure 14: Mean drag coefficient C_x (filled black circles) and conditional averaging based on the sign (N negative and P positive) of the vertical pressure gradient (thick lines) for the Berlingo in pitch variations and the Partner in yaw variations.

restore the P state for the closed air-intake configuration to further improve the 3.7% of drag reduction of the Kangoo. This practical test is investigated in the following as a demonstration of the beneficial impact of controlling the z-instability.

3.4. Manipulation of the instability

A global trend is highlighted above: closing the air-intake is an efficient drag reduction technique –

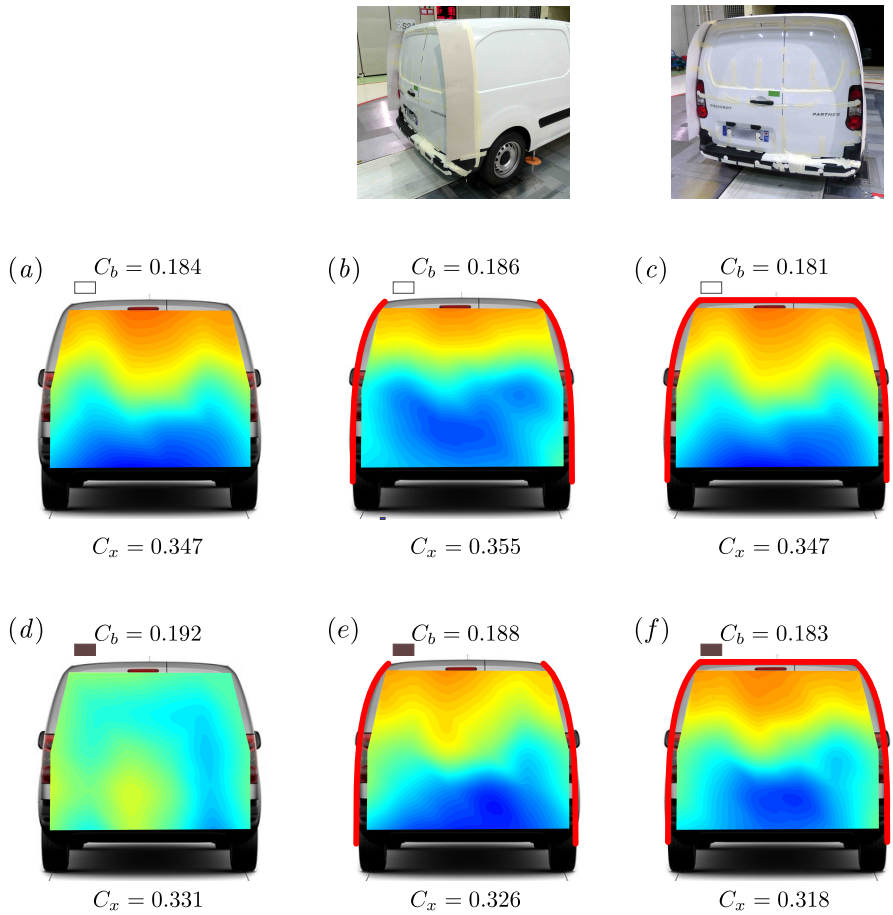

Figure 15: Mean base pressure distribution $C_p(y^*, z^*)$ for the Peugeot Partner at $\Delta\alpha = 2.3°$ and associated mean base suction and drag coefficients C_b and C_x: (a) Open air-intake without control, (b) closed air-intake without control, (c) side plates and closed air-intake, (d) side plates and open air-intake, (e) base cavity and closed air-intake, (f) base cavity and open air-intake. The red lines model the control devices installed on the vehicle.

applicable in real driving conditions when the need for engine cooling is low – but would potentially trigger the reversed state N. The state N has poor aerodynamic performance compared to the P state with both a higher base suction increasing drag and a higher lift reducing the vehicle's stability, especially at high driving speeds. The purpose of this section is then to manipulate the wake when in state N in order to retrieve the more efficient state P by simple geometrical modifications.

The passive flow control devices we have chosen for the Partner are inspired from the base cavity effect investigated by [5]. We consider two vertical plates at the both sides of the base and an additional third plate at the roof as illustrated at the top in figure 15. The length of each plate equals the side length they are associated with and the width is $d = 0.3$ m, *i.e.* $d^* = d/H = 0.203$. The Partner is placed in pitching conditions at $\alpha = 2.3°$ to obtain a permanent state P with open air-intake and a permanent state N with closed air intake similarly to what was obtained for the Berlingo in the previous sections. These two states can indeed be identified in the corresponding base pressure distribution given in figure 15(a) for open air-intake and figure 15(d) for closed air-intake. We can see that the state N has a large base suction of $C_b = 0.192$ compared to that of $C_b = 0.184$ of the P state while the drag has decreased by 4.6% by avoiding the airflow through the vehicle. The side plates degrade the base suction and the drag for the open air intake configuration in figure 15(b) but produce a permanent P state in figure 15(e) which significantly reduces base suction and drag.

The best definitive passive device is with the additional roof plate where drag remains unchanged for open air intake in figure 15(c) compared to no device at all in figure 15(a) and reduced by 8.3% in figure 15(f) compared with open air intake and no device at all in figure 15(a). Thus the drag reduction of 4.3% obtained by closing the air intake is improved to 8.3% with an additional passive device controlling the instability without modifying the drag with open air-intake.

4. Discussion and conclusion

This paper is focused on the wake dynamics of blunt based real ground vehicles. Their wakes, in the baseline configuration – aligned with the flow at a natural ground clearance – exhibit a strong asymmetry in the vertical direction that is not only related to the shape asymmetry nor to the presence of the road. The cars are indeed found to be subjected to a z-instability of the wake in the sense of [14] despite the aspect ratio of their base.

Similar wake transitions as those observed with the Ahmed body subjected to the z-instability [19] are identified with these vehicles when the ground clearance, the yaw or the pitch angles are modified. This indicates the relevance of fundamental studies for industrial applications since the implied mechanisms are identical. The impact of these transitions on the aerodynamic loading is also found similar, with a clear correlation between the base pressure gradients and the cross-flow loading not only in mean but also in instantaneous values since the fluctuations of the base pressure distribution directly impact those of the cross-flow loading, with a shape-dependent factor of proportionality.

Two wake states are identified and characterized by different strength which is ascribed to the strong asymmetries between the top and the bottom of the vehicles; the impact of the wheels wake is visible in the reversed wake state and also contributes to the different strengths. Wake reversals have shown to be not only sensitive to the vehicle's alignment but also to the flow underneath which can be controlled by the air-intake system or underbody roughness. However, we show in this paper that simple manipulations of the flow such as a rear cavity or a rear spoiler provide easy-to-implement solutions which lead to satisfactory results. Nonetheless, the largest drag reduction should be achieved by removing the instability and stabilizing the flow on the symmetric wake state.

Acknowledgments

The authors wish to thank the *Centre National de Recherche Technologique de Recherche en Aerodynamique et Aroacoustique des Vhicules terrestres* (CNRT R2A) for funding this work as well as Groupe PSA and Groupe Renault for providing the vehicles. We acknowledge the staff of the GIE-S2A for the support during the test sessions.

References

[1] S. Ahmed, G. Ramm, G. Faitin, Some salient features of the time-averaged ground vehicle wake, SAE Technical Paper Series 840300.

[2] M. Grandemange, M. Gohlke, O. Cadot, Reflectional symmetry breaking of the separated flow over three-dimensional bluff bodies, Physical Review E 86 (2012) 035302.

[3] M. Grandemange, M. Gohlke, O. Cadot, Turbulent wake past a three-dimensional blunt body. Part 1. Global modes and bi-stability., Journal of Fluid Mechanics 722 (2013) 51–84.

[4] R. Volpe, P. Devinant, A. Kourta, Experimental characterization of the unsteady natural wake of the full-scale square back Ahmed body: flow bi-stability and spectral analysis, Experiments in Fluids 56 (5).

[5] A. Evrard, O. Cadot, V. Herbert, D. Ricot, R. Vigneron, J. Délery, Fluid force and symmetry breaking modes of a 3D bluff body with a base cavity, Journal of Fluids and Structures 61 (2016) 99–114.

[6] A. Perry, G. Pavia, M. Passmore, Influence of short rear end tapers on the wake of a simplified square-back vehicle: wake topology and rear drag, Experiments in Fluids 57 (11) (2016) 169. doi:10.1007/s00348-016-2260-3.

[7] R. Li, D. Barros, J. Borée, O. Cadot, B. R. Noack, L. Cordier, Feedback control of bimodal wake dynamics, Experiments in Fluids 57 (10) (2016) 158.

[8] R. D. Brackston, J. García De La Cruz, A. Wynn, G. Rigas, J. F. Morrison, Stochastic modelling and feedback control of bistability in a turbulent bluff body wake, Journal of Fluid Mechanics 802 (2016) 726749. doi:10.1017/jfm.2016.495.

[9] E. Varon, Y. Eulalie, S. Edwige, P. Gilotte, J.-L. Aider, Chaotic dynamics of large-scale structures in a turbulent wake, Physical Review Fluids 2 (2017) 034604.

[10] D. Barros, J. Borée, O. Cadot, A. Spohn, B. R. Noack, Forcing symmetry exchanges and flow reversals in turbulent wakes, Journal of Fluid Mechanics 829. doi:10.1017/jfm.2017.590.

[11] R. Pasquetti, N. Peres, A penalty model of synthetic micro-jet actuator with application to the control of wake flows, Computers & Fluids 114 (0) (2015) 203–217.

[12] J.-M. Lucas, O. Cadot, V. Herbert, S. Parpais, J. Délery, A numerical investigation of the asymmetric wake mode of a squareback Ahmed body effect of a base cavity., Journal of Fluid Mechanics 831 (1) (2017) 675 – 697.

[13] O. Evstafyeva, A. S. Morgans, L. Dalla Longa, Simulation and feedback control of the ahmed body flow exhibiting symmetry breaking behaviour, Journal of Fluid Mechanics 817. doi:10.1017/jfm.2017.118.

[14] M. Grandemange, M. Gohlke, O. Cadot, Bi-stability in the turbulent wake past parallelepiped bodies with various aspect ratios and wall effects, Physics of Fluids 25 (2013) 95–103.

[15] M. Grandemange, O. Cadot, A. Courbois, V. Herbert, D. Ricot, T. Ruiz, R. Vigneron, A study of wake effects on the drag of the Ahmed squareback model at the industrial scale, Journal of Wind Engineering and Industrial Aerodynamics 145 (2015) 282–291.

[16] O. Cadot, A. Evrard, L. Pastur, Imperfect supercritical bifurcation in a three-dimensional turbulent wake, Physical Review E 91 (6).

[17] T. Castelain, M. Michard, M. Szmigiel, D. Chacaton, D. Juv, Identification of flow classes in the wake of a simplified truck model depending on the underbody velocity, Journal of Wind Engineering and Industrial Aerodynamics 175 (2018) 352–363. doi:10.1016/j.jweia.2018.02.004.

[18] H.-J. Schmidt, R. Woszidlo, C. N. Nayeri, C. O. Paschereit, The effect of flow control on the wake dynamics of a rectangular bluff body in ground proximity, Exp. Fluids 59 (6) (2018) 107. doi:10.1007/s00348-018-2560-x.

[19] G. Bonnavion, O. Cadot, Unstable wake dynamics of rectangular flat-backed bluff bodies with inclination and ground proximity, J. Fluid Mech.

[20] O. Cadot, A. Courbois, D. Ricot, T. Ruiz, F. Harambat, V. Herbert, R. Vigneron, J. Délery, Characterisations of force and pressure fluctuations of real vehicles, Int. J. Engineering Systems Modelling and Simulation 8 (2) (2016) 99–105.

[21] G. Bonnavion, O. Cadot, A. Évrard, V. Herbert, S. Parpais, R. Vigneron, J. Délery, On multistabilities of real car's wake, Journal of Wind Engineering and Industrial Aerodynamics 164 (2017) 22–33.

[22] G. Pavia, M. Passmore, Characterisation of Wake Bistability for a Square-Back Geometry with Rotating Wheels, in: J. Wiedemann (Ed.), Progress in Vehicle Aerodynamics and Thermal Management, Springer International Publishing, 2018, pp. 93–109.

[23] P. Waudby-Smith, T. Bender, R. Vigneron, The GIE S2A full-scale aeroacoustic wind tunnel, SAE Technical Paper Series 2004-01-0808.